Journal of Materials Science: Materials in Electronics (2019) 30:17682–17692
https://doi.org/10.1007/s10854-019-02118-x

Effect of CdS shell thickness on the photocatalytic properties of TiO_2@CdS core–shell nanorod arrays

Zhu Shi[1] · Jiani Liu[1] · Huixia Lan[2] · Xiuyan Li[1] · Bangyao Zhu[3] · Jinghai Yang[1]

Received: 2 July 2019 / Accepted: 27 August 2019 / Published online: 3 September 2019

Abstract

Rutile TiO_2 nanorod arrays (NRAs) with average diameter approximately 80 nm were first synthesized by solvothermal method using Ti foil as both titanium source and substrate. And then TiO_2@CdS core–shell heterostructure NRAs were fabricated via subsequent successive ionic layer adsorption and reaction (SILAR) route using the TiO_2 NRAs as precursor. The thicknesses of CdS shell varied from 4 to 18 nm by changing the times of SILAR cycle. The photocatalytic performances of pure TiO_2 and all TiO_2@CdS NRAs were investigated on the degradation of rhodamine B (RhB) aqueous solution under simulated sunlight irradiation. Compared to pure TiO_2 NRAs, all TiO_2@CdS NRAs displayed superior photocatalytic activities, and the optimal CdS shell thickness of TiO_2@CdS NRAs was about 11 nm. A possible Z-scheme electron transfer mechanism for TiO_2@CdS NRAs nanocomposite with the enhanced photocatalytic performance was provided.

1 Introduction

It is well known that water is the source of life, which is an indispensable part of human beings, animals and plants. In recent years, the serious problem of water pollution has been caused by garbage pollution, textile wastewater and other pollution sources [1, 2]. Numerous techniques have been devoted to treat sewage water pollution, such as electrochemical degradation, micellar enhanced ultra-filtration, adsorption or microbial degradation, and photocatalysis [3, 4]. Among them, photocatalysis technology has been regarded as one of the most promising methods in the field of sewage treatment because of the advantages of simple equipment, easy operation, low energy consumption and no secondary pollution [5–7].

Titanium dioxide (TiO_2), as an important photocatalyst with the advantages of excellent chemical stability, high catalytic reactivity, low cost and non-toxicity, has been widely researched in the field of the sewage water pollution [8–10]. There are three mainly distinct crystalline structures of TiO_2: anatase, rutile and brookite [11, 12]. Among them, anatase TiO_2 (a-TiO_2) has been recognized that it exhibits higher photocatalytic activity than other crystalline structures [13]. However, the relatively wide band gap of a-TiO_2 (3.2 eV) can only be excited by the UV light, which directly limits the practical application of it in the field of the photocatalysis. [14–16]. Recently, some researches indicate that rutile TiO_2 (r-TiO_2) exhibits unexpectedly properties [17, 18]. In addition, Mohammadpour et al. reported the passivation carrier mobility on the surface of rutile TiO_2 was increased by 100-fold [19]. Thakur et al. discussed hydrothermally grown rutile TiO_2 has the advantage of optimizing charge transfer with high contact area in halide perovskite solar cells [20]. Therefore, r-TiO_2 is of research value in charge transfer and carrier migration, which is also an indispensable advantage for photocatalysis. Furthermore, r-TiO_2 with the direct band gap of 3.0 eV can absorb the wavelength of sunlight below 410 nm. This is to say, r-TiO_2 can be excited by a part of visible light. Therefore, the research of preparation and photocatalytic activity of the r-TiO_2 becomes a research hotspot in these years.

Electronic supplementary material The online version of this article (https://doi.org/10.1007/s10854-019-02118-x) contains supplementary material, which is available to authorized users.

✉ Xiuyan Li
lixiuyan@jlnu.edu.cn

[1] Key Laboratory of Functional Materials Physics and Chemistry of the Ministry of Education, Jilin Normal University, Changchun 130103, People's Republic of China

[2] College of Environment and Safe Engineering, Qingdao University of Science & Technology, Qingdao 266042, Shandong, People's Republic of China

[3] Department of Tourism and Geography, Jilin Normal University, Siping 136000, Jilin, People's Republic of China

Relatively fast recombination of photogenerated electron–hole pairs is an obvious inherent drawback of conventional single material photocatalyst. Design and preparation of heterojunction composite photocatalyst is an effective strategy for promoting photogenerated carrier separation and transportation [21, 22]. Recent studies manifest that the photocatalytic activity can be enhanced dramatically by coupling TiO_2 with other semiconductors, compared to its individual counterpart [23–25]. As a typically narrow band gap semiconductor, CdS (2.4 eV) is widely used to prepare the heterojunction composite photocatalyst due to the great visible light absorption ability of it [26, 27]. It has been suggested that the CdS/TiO_2 system has a matched band structure and complementary optical properties. At present, the CdS@TiO_2 core–shell structure has been obtained through different methods [28, 29]. In contrast, some a-TiO_2/CdS composites have also been synthesized [30–32], and corresponding experiments results show that the photogenerated carriers easily transfer in TiO_2/CdS composite due to the difference in the energy band levels between TiO_2 and CdS. However, the preparation and photocatalytic performance of r-TiO_2/CdS composites is studied rarely. In addition, TiO_2 in the form of film displays obvious virtue in separating from the reaction system and recycling in photocatalytic reaction, compared with other forms of TiO_2 [33, 34]. Moreover, it is novel and interesting to study the influence of shell thickness on photocatalytic activity and the effect of Z-scheme heterojunction on the photogenerated carrier transport behavior between interfaces of the nanocomposite [35–37]. Therefore, synthesizing r-TiO_2@CdS core–shell NRAs with the different CdS shell thicknesses and study of their photocatalytic performances are significant.

In this paper, TiO_2@CdS NRAs with different CdS shell thicknesses were fabricated via solvothermal method and subsequent successive ionic layer adsorption and reaction (SILAR) route. The geometrical morphologies, microstructures and optical properties of the pure TiO_2 and all TiO_2@CdS NRAs were investigated by XRD, SEM, TEM, XPS and UV–Vis DRS. The photocatalytic activities of pure TiO_2 and TiO_2@CdS NRAs with different CdS shell thicknesses were compared by the photodegradation process of RhB aqueous solution under simulated sunlight irradiation. Furthermore, the possible photocatalytic mechanism was proposed.

2 Experimental section

2.1 Synthesis

Preparation of TiO_2 NRAs. HCl is a widely recognized corrosive agent that affects the hydrolysis process of Ti foil to form TiO_2. In the hydrothermal process, rutile TiO_2 seed layer is influenced by the concentration of HCl on the chemical corrosion of Ti substrate [38]. Rutile TiO_2 NRAs were synthesized by solvothermal route using the Ti foil as both substrate and titanium source. The commercial Ti foil with dimension of 9 mm × 9 mm was cleaned by sonication successively in ethanol and deionized water. Then, Ti foil was put into a 30 mL Teflon-lined autoclave with 10 mL of HCl (0.5 mol L^{-1}), and this system was maintained at 180 °C for 24 h. After cooling to room temperature, the film was thoroughly rinsed with deionized water and then dried in a desiccator.

Preparation of TiO_2@CdS NRAs. TiO_2@CdS core–shell heterostructure NRAs were synthesized by the SILAR way using the as-prepared rutile TiO_2 NRAs as precursor. In a typical procedure, the as-synthesized TiO_2 NRAs were separately placed into 0.06 mol L^{-1} $Cd(NO_3)_2$ and 0.06 mol L^{-1} Na_2S aqueous solution for 3 min at room temperature with slowly shaking. $Cd(NO_3)_2$ and Na_2S supply Cd^{2+} ions and S^{2-} ions, respectively. During each immersion interval, TiO_2 NRAs were thoroughly rinsed with deionized water to dislodge the redundant ions from the surface of them. Different CdS shell thicknesses were fabricated via changing the times of SILAR cycle. For brevity, the prepared samples with 3, 6 and 9 times of SILAR cycle were labeled as TiO_2@CdS-3, TiO_2@CdS-6 and TiO_2@CdS-9, respectively. The synthetic procedure of TiO_2 and TiO_2@CdS NRAs are shown in Scheme 1.

2.2 Characterizations

The crystal structure and phase component were investigated using X-ray diffraction (XRD, Rigaku-D/max-2500 diffractometer, Japan). The geometrical morphologies and microstructures were determined by a field emission scanning electron microscope (FE-SEM, JEOL 7800F, Japan) and transmission electron microscope (TEM, FEI Tenai G2 F20, USA). The elemental compositions and chemical status were analyzed by X-ray photoelectron spectroscopy (XPS, Thermo Scientific ESCALAB 250Xi A1440 system, USA). UV–Vis diffuse reflectance spectra (UV–Vis DRS) were obtained on a spectrometer (Perkin-Elmer Lambda 900, USA) using magnesium oxide as a standard. The Raman spectra of the samples were measured (Horiba-Jobin-Yvon LabRAM ARAMIS). The optical properties were observed by photoluminescence spectra (PL, Renishaw inVia micro-PL spectrometer) at room temperature. Electron spin resonance (ESR) was performed on the ESR spectrometer (Brucker, A300).

2.3 Photocatalytic experiment

Rhodamine B (RhB) water solution was used as a target pollutant to explore the photocatalytic activities of samples under simulated sunlight which was provided by a 300 W

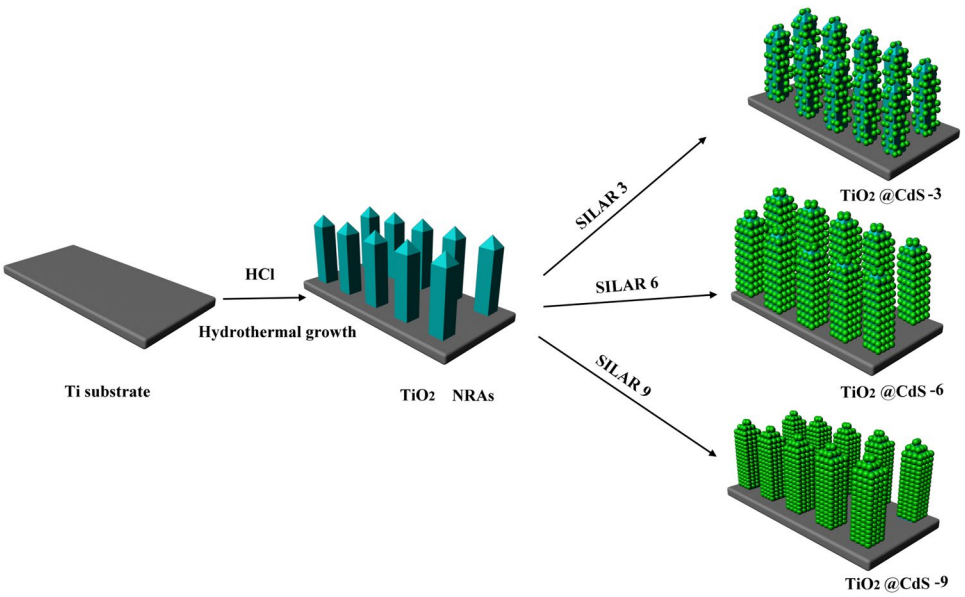

Scheme 1 Synthetic procedure of rutile TiO_2 NRAs and TiO_2@CdS on Ti substrate

Xe lamp (CEL-HXF300). In a typical procedure, the sample was immersed into a rectangular quartz cuvette containing 2 mL RhB water solution (2 mg L^{-1}). Prior to irradiation, the reaction system was placed in dark for 15 min to set up the equilibrium of adsorption–desorption. After a certain period of time, the absorbance spectrum of RhB water solution was analyzed by UV–Vis spectrophotometer (UV-5800PC, China). Repeated photocatalytic tests were executed under the identical experiment circumstance to investigate the reusability of the photocatalyst. The photocatalyst was only washed with deionized water after cycling photocatalytic experiment, and then was used for the next cycle of degradation.

3 Results and discussion

Figure 1 shows the SEM images of pure TiO_2 and all TiO_2@CdS NRAs. All samples are rod-like and grew on Ti substrate. Figure 1a shows the SEM image of pure TiO_2 NRAs. All TiO_2 rods display smooth surface and the average diameter is approximately 80 nm. Furthermore, TiO_2 nanorods are cubic and the top facets are pyramid. Figures 2b-d show the SEM images of TiO_2@CdS-3, TiO_2@CdS-6 and TiO_2@CdS-9, respectively. Clearly, the diameters of TiO_2@CdS NRAs increase with the increasing of SILAR cycle times, and the surfaces of all TiO_2@CdS nanorods are getting rough.

Figures 2a, c, e and g show the TEM images of a sole TiO_2, TiO_2@CdS-3, TiO_2@CdS-6 and TiO_2@CdS-9 rod, respectively. Those TEM images reveal that the mean length of those nanorods is around 350 nm. The profile of pure TiO_2 nanorod is smooth, while the outlines of all TiO_2@CdS nanorods are rough. This is in good coincident with the SEM observation from Fig. 1. The HRTEM image of pure TiO_2 in Fig. 2b exhibits that the lattice fringes of 0.325 and 0.295 nm are separately consisting with the (110) plane and (001) plane of rutile TiO_2. Meanwhile, the HRTEM result also indicates that TiO_2 nanorod is single-crystalline nature, and grew along <001> direction. The interplanar distance of 0.206 (Fig. 2d), 0.291 (Fig. 2f, h) and 0.336 nm (Fig. 2f, h) are matching to the (220), (200) and (111) planes of cubic CdS, respectively. In addition, Figs. 2d, f and g show that the CdS shell thickness of TiO_2@CdS-3, TiO_2@CdS-6 and TiO_2@CdS-9 are separately about 4 nm, 11 nm and 18 nm, respectively.

Figure 3 presents the XRD patterns of Ti foil, pure TiO_2 and all TiO_2@CdS NRAs. Besides some peaks belonging to Ti (JCPDS card No. 87-0713) foil, four main diffraction peaks at 27.4°, 41.2°, 54.3° and 69.0° of pure TiO_2 NRAs are observed in Fig. 3b, which are separately corresponding to the (110), (111), (211) and (301) planes of rutile TiO_2 (JCPDS card No. 21-1276). Figures 3c–e show the XRD patterns of TiO_2@CdS-3, TiO_2@CdS-6 and TiO_2@CdS-9 NRAs, respectively. No obvious characteristic peaks originating from CdS are detected in Figs. 3c, d, suggesting that the thickness of CdS shell layer are relatively thin in TiO_2@CdS-3 and TiO_2@CdS-6 NRAs. Three diffraction peaks at about 26.5°, 43.9° and 52.1° in Fig. 3e belonging to (111), (220) and (311) planes of cubic CdS (JCPDS card No. 26-0339) are detected clearly in the sample of TiO_2@CdS-9, implying that the thickness of CdS shell layer in TiO_2@CdS-9 is higher than other samples. This result confirms the SEM and TEM results.

Since the characteristic peaks of CdS in XRD are not obvious, Raman spectra were used to characterize all

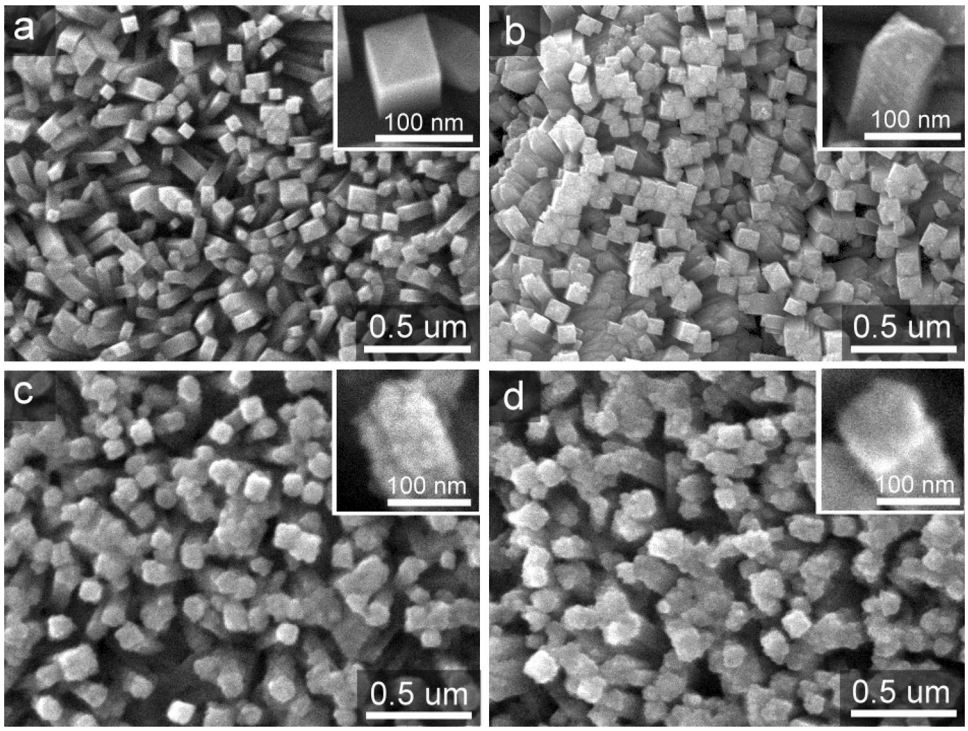

Fig. 1 SEM images of **a** TiO_2, **b** TiO_2@CdS-3, **c** TiO_2@CdS-6 and **d** TiO_2@CdS-9 NRAs

samples in order to better explain the composition of phases. The Raman spectra of TiO_2 and all TiO_2@CdS NRAs are presented in Fig. 4. The characteristic vibration Raman peaks at 246, 437 and 607 cm^{-1} ascribed to the E_g and A_{1g} active mode vibrations of rutile phase TiO_2 [39, 40]. In addition, a clear vibration peak at about 301 cm^{-1} can be noticed for the TiO_2@CdS NRAs, which corresponding to the fundamental longitudinal optical (LO) phonon of CdS cubic phase [41]. Raman spectroscopy results complement the shortcomings of XRD.

Figure 5 shows the XPS spectrum of TiO_2@CdS-6 NRAs. The full spectrum in Fig. 5a clearly displays the peaks of Ti, O, Cd, S and C elements. The emergence of C peak originates from the signal of carbon of XPS device [42]. Figure 5b exhibits Ti 2p XPS spectrum. Two peaks located at 458.5 eV and 464.2 eV are assigned to the Ti $2p_{3/2}$ and the Ti $2p_{1/2}$ binding energies, respectively. The peak splitting between the Ti $2p_{3/2}$ and Ti $2p_{1/2}$ is 5.7 eV, indicating the existence of Ti^{4+} state in TiO_2@CdS-6 NRAs [43, 44]. Figure 4c shows two main peaks at 529.7 eV and 532.1 eV. The first peak originates from crystal lattice oxygen of TiO_2 [45, 46]. And the second peak belongs to oxygen in hydroxyl groups (–OH) [47]. As shown in Figs. 4d, the binding energies of Cd $3d_{5/2}$ and Cd $3d_{3/2}$ located at 405.1 eV and 411.8 eV, respectively, indicating that Cd exists in the form of Cd^{2+} [48–50]. For the spectrum of S 2p (in Fig. 4e), two peaks at 161.3 eV and 162.8 eV are separately accounted for S $2p_{3/2}$ and S $2p_{1/2}$, indicating that S element existed in the form of S^{2-} [51, 52]. In short, the XPS result further confirms that Ti, O, Cd and S elements exist simultaneously in TiO_2@CdS-6 NRAs.

Figure 6 shows the UV–Vis DRS of pure TiO_2, CdS nanoparticle, TiO_2@CdS-3, TiO_2@CdS-6 and TiO_2@CdS-9 NRAs. Pure TiO_2 NRAs exhibit absorption in the wavelength below 410 nm due to the intrinsic band gap of rutile TiO_2. The UV–Vis DRS of TiO_2@CdS-3 and pure TiO_2 NRAs are similar. This is because the thickness of CdS shell layer in TiO_2@CdS-3 NRAs is very thin. Compared to pure TiO_2 NRAs, the absorption of TiO_2@CdS-6 and TiO_2@CdS-9 NRAs has a weak red shift. Furthermore, both TiO_2@CdS-6 and TiO_2@CdS-9 display obviously enhanced light absorption abilities in the visible region comparing to pure TiO_2 NRAs. The absorption intensity in the visible region of TiO_2@CdS-9 is stronger than that of TiO_2@CdS-6 owing to the relatively thick CdS shell layer in TiO_2@CdS-9 NRAs. The band gap (E_g) value is calculated on the basis of the formula: $\alpha h\nu = (h\nu - E_g)^n$ [53]. As shown in Fig. 6b, the E_g values of TiO_2, CdS, TiO_2@CdS-3, TiO_2@CdS-6 and TiO_2@CdS-9 are 3.02, 2.15, 3.01, 2.99 and 2.95 eV, respectively. This indicates that these E_g values of TiO_2@CdS core–shell heterostructure NRAs strongly depend on the CdS shell thickness.

Photoluminescence (PL) technology is an important means to study semiconductor impurities and defects, and has important application value in the field of photocatalysis. Figure 7 showed PL spectra of all samples excited in 325 nm. The main emission peaks of these samples cover 500–600 nm region. And the deep-level emission came

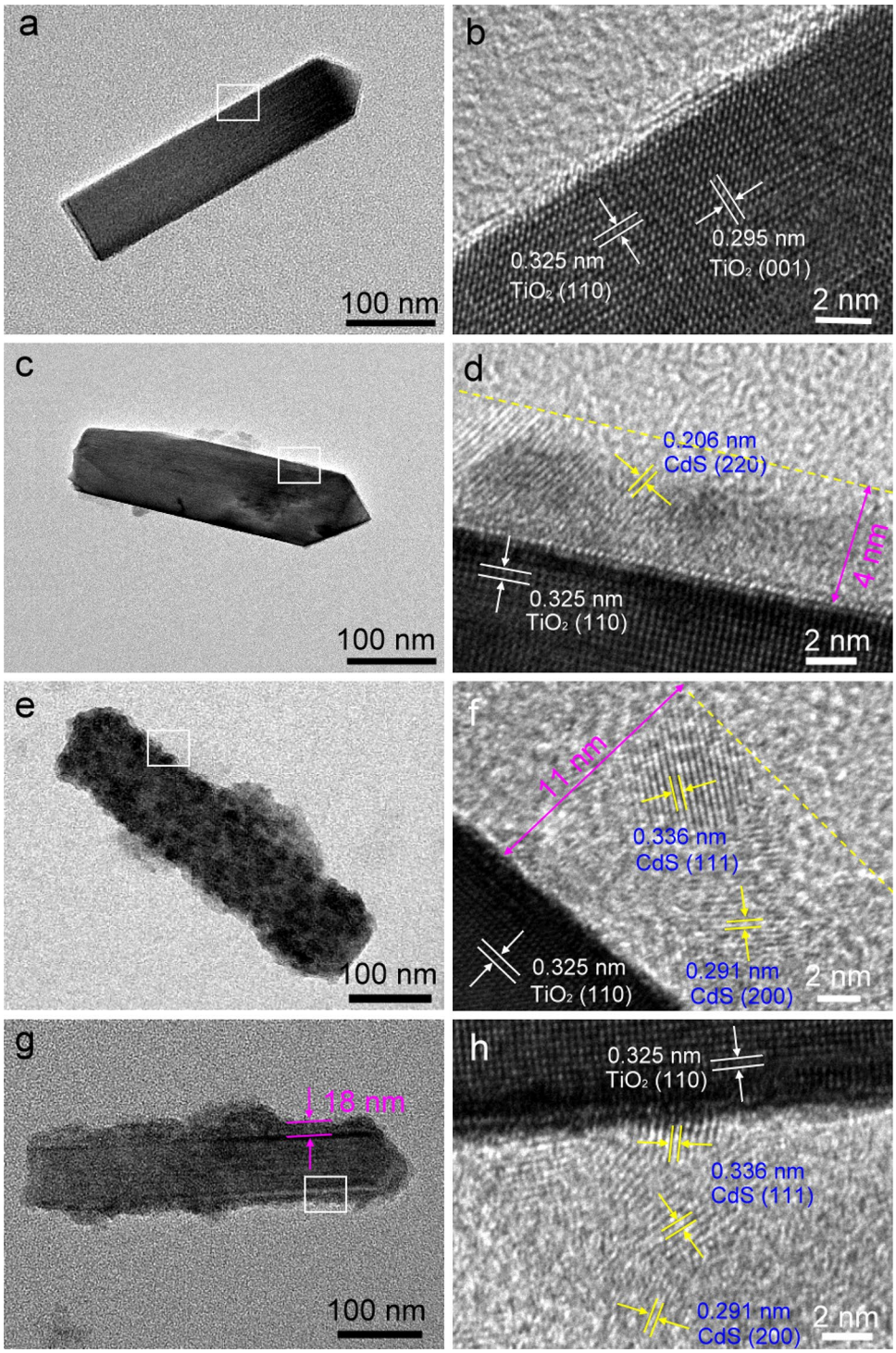

Fig. 2 TEM and HRTEM images of **a**, **b** TiO_2, **c**, **d** TiO_2@CdS-3, **e**, **f** TiO_2@CdS-6 and **g**, **h** TiO_2@CdS-9 NRAs

from the surface defects of samples [54]. The fluorescence intensity in Fig. 7 shows that TiO_2@CdS-6 has the highest PL intensity. Obviously, it is reasonable to modify TiO_2 NRAs by CdS, which can drastically increase the PL intensity of pure TiO_2. The results show that the higher the defect concentration, the capture of photoelectrons leads to the improvement of carrier separation efficiency. That is to say, with a high surface defect concentration of CdS, it can be used as an electron trap and photocatalytic reactive site to capture part of the electrons transported by TiO_2 and participate in the reaction, and the other part is involved in luminescence. Therefore, the higher defect concentration is beneficial to the photocatalytic reaction [55, 56].

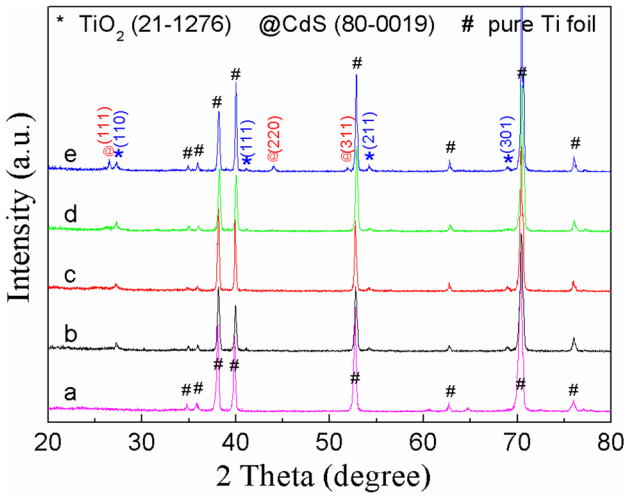

Fig. 3 XRD patterns of (a) pure Ti foil, (b) TiO_2, (c) TiO_2@CdS-3, (d) TiO_2@CdS-6 and (e) TiO_2@CdS-9 NRAs

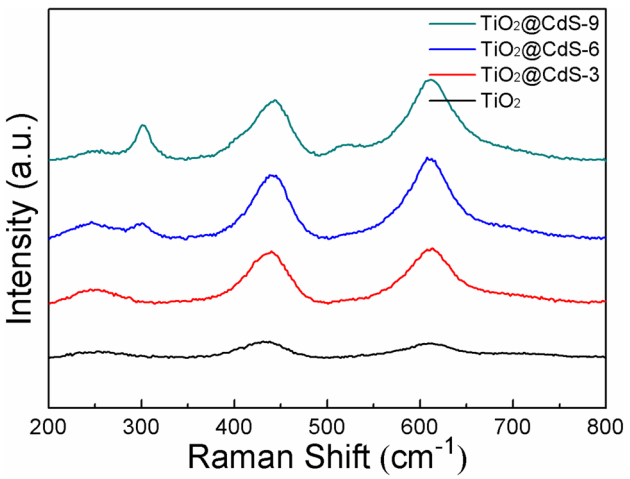

Fig. 4 Raman spectra of TiO_2 and TiO_2@CdS NRAs

In order to prove that the heterojunction between the TiO_2 and CdS is benefit for the photocatalytic performance, the TiO_2@SiO_2 and TiO_2@SiO_2@CdS-6 NRAs were prepared and the SEM images of these nanocomposites were shown in Figs. S1 and S2. And the photocatalytic activity of TiO_2@CdS was compared with pure TiO_2 and TiO_2@SiO_2@CdS NRAs. In the photocatalytic experiment, SiO_2 is inert and the CdS becomes the bare layer in TiO_2@SiO_2@CdS-6. The photocatalytic activities of TiO_2, TiO_2@SiO_2@CdS-6, and all TiO_2@CdS NRAs are evaluated by the photodegradation experiments of RhB aqueous solution under simulated solar light irradiation, and the corresponding results are shown in Fig. 8a. Obviously, blank experiment reveals that the photolysis of RhB aqueous solution can be omitted in the absence of photocatalyst. After 120 min irradiation, 38.0% and 53.1% RhB water solution are photodegraded by pure TiO_2 NRAs and TiO_2@SiO_2@CdS-6, respectively. Whereas 84.7%, 96.6% and 92.2% RhB water solutions is photodegraded using TiO_2@CdS-3, TiO_2@CdS-6 and TiO_2@CdS-9 as photocatalyst, respectively. The photocatalytic activities of the prepared samples under simulated solar light irradiation show the following order: TiO_2@CdS-6 > TiO_2@CdS-9 > TiO_2@CdS-3 > TiO_2@SiO_2@CdS-6 > TiO_2. Namely, all TiO_2@CdS NRAs exhibit higher photocatalytic activity than pure TiO_2 NRAs and TiO_2@SiO_2@CdS-6. In addition, the photocatalytic activities of TiO_2@CdS NRAs strongly depend on the thickness of CdS shell.

The reaction rate constant (k, min^{-1}) is investigated via the first order kinetic kinetics equation $\ln(C_0/C) = kt$ [57, 58]. And C_0 and C on behalf of the real-time and initial concentrations of RhB, respectively. Figure 8b illustrates the k values of TiO_2 and all TiO_2@CdS NRAs. It is quite clear that TiO_2@CdS-6 NRAs owns the biggest k value among all as-synthesized samples, while the pure TiO_2 NRAs possesses the smallest k value. And the k value of TiO_2@CdS-6 NRAs is around 6.6 and 3.6 times than that of pure TiO_2 NRAs and TiO_2@SiO_2@CdS-6 NRAs, respectively. As shown in Fig. 8c, we can notice that the efficiency of the TiO_2@CdS-6 degradation curve for RhB dye ranges from 0 to 120 min under simulated solar light irradiation. The true color change of RhB aqueous are inset in Fig. 8c. As the reaction time goes on, the color of RhB aqueous solution becomes lighter. The reusability of TiO_2@CdS-6 NRAs is evaluated in recycling reaction. The corresponding result is shown in Fig. 8b. According to Fig. 8b, the photocatalytic efficiency reaches to 93.7% after five successive cycles, demonstrating that TiO_2@CdS-6 NRAs exhibit good reusability. This result also indicates that CdS nanoparticles are firmly attached to TiO_2 nanorods.

It is widely accepted that mainly three reactive species including hydroxyl radicals ($^{\cdot}OH$), photogenerated hole (h^+) and superoxide anion radical ($^{\cdot}O^{2-}$) are involved during the photocatalytic reaction. In order to explore the mechanism of photodegradation reaction, the trapping experiments of reactive species are executed using the TiO_2@CdS-6 NRAs as photocatalyst. Three quenchers, ethylenediaminetetraacetate (EDTA), *tert*-butyl alcohol (*t*-BuOH) and benzoquinone (BQ) are employed to capture h^+, $^{\cdot}OH$, and $^{\cdot}O^{2-}$, respectively [59–61]. The result in Fig. 9 shows that three quenchers lead to the fast deactivation of TiO_2@CdS-6 NRAs. After adding BQ, EDTA and *t*-BuOH, the degradation rate of RhB water solution decreases from 96.6% to 36.0% (BQ), 24.2% % (EDTA) and 42.9% (*t*-BuOH), respectively, indicating that $^{\cdot}O^{2-}$, h^+ and $^{\cdot}OH$ play the important roles in the photocatalytic process.

Electron spin resonance (ESR) spectra were applied to further investigate the superoxide and hydroxyl radicals generated under simulated solar light. 5,5-Dimethyl-1-pyrroline N-oxide (DMPO), as a trap agent, is dispersed

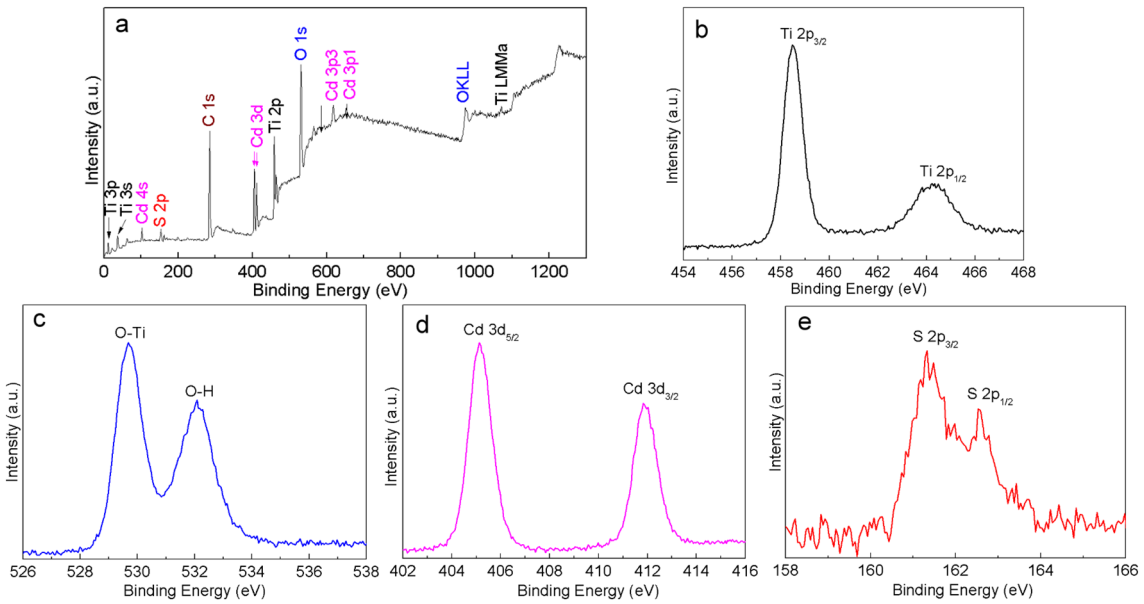

Fig. 5 XPS spectra of TiO_2@CdS-6 NRAs: **a** survey spectrum, **b** Ti 2p, **c** O 1s, **d** Cd 3d and **e** S 2p

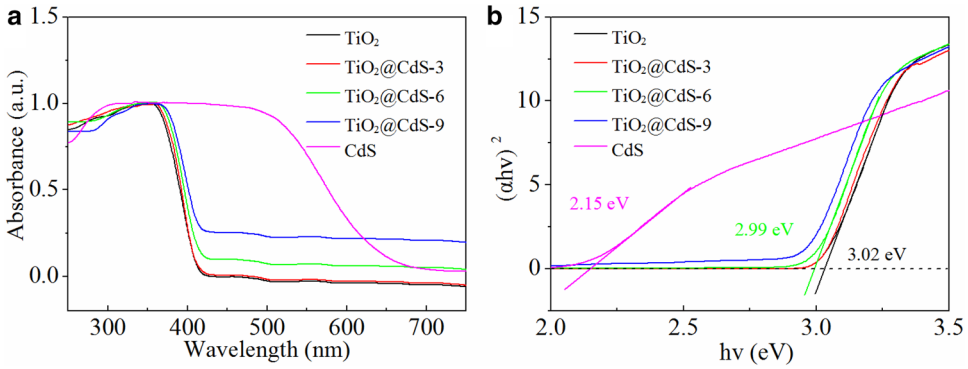

Fig. 6 **a** UV–Vis DRS and **b** plot of $(\alpha h\nu)^2$ versus $(h\nu)$ of TiO_2 and all TiO_2@CdS NRAs

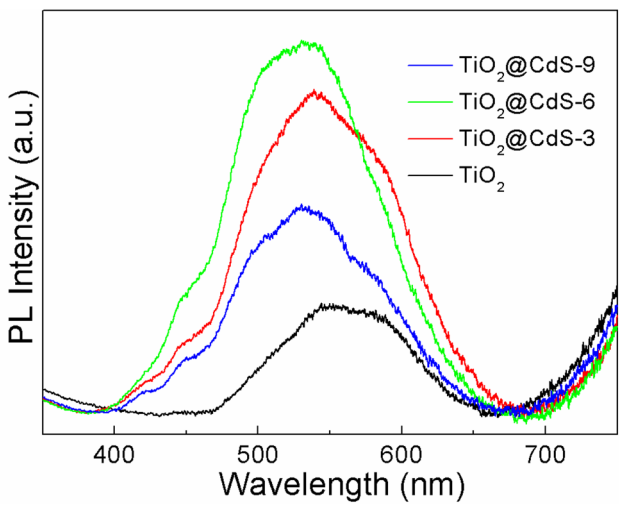

Fig. 7 Room-temperature PL spectra of TiO_2 and all TiO_2@CdS NRAs

in a methanol and water solution [35, 62]. As illustrated in Fig. 10a, b, no obvious DMPO–$^{\cdot}O^{2-}$ and DMPO–$^{\cdot}OH$ signals are detected under darkness. However, characteristic peaks of DMPO–$^{\cdot}O^{2-}$ and DMPO–$^{\cdot}OH$ were observed under simulated solar light irradiation. This indicating that the presence of $^{\cdot}O^{2-}$ and $^{\cdot}OH$ radicals after simulated solar light irradiation. The ESR analysis is consistent with the results of species trapping experiments.

The superior photocatalytic activity of TiO_2@CdS NRAs is attributed to the synergistic effect of TiO_2 and CdS, which is favorable for the segregation of photoinduced electron–hole pairs. Figure 11 illustrates the possible photocatalytic mechanism of TiO_2@CdS NRAs, and there are two possible ways for the transfer of photoinduced carriers. Under simulated sunlight illumination, both TiO_2 and CdS can be excited to produce photoinduced electrons and holes. Usually, the photoinduced electrons from CdS will migrate to TiO_2, and the holes of TiO_2 will move to CdS because of the stepwise band

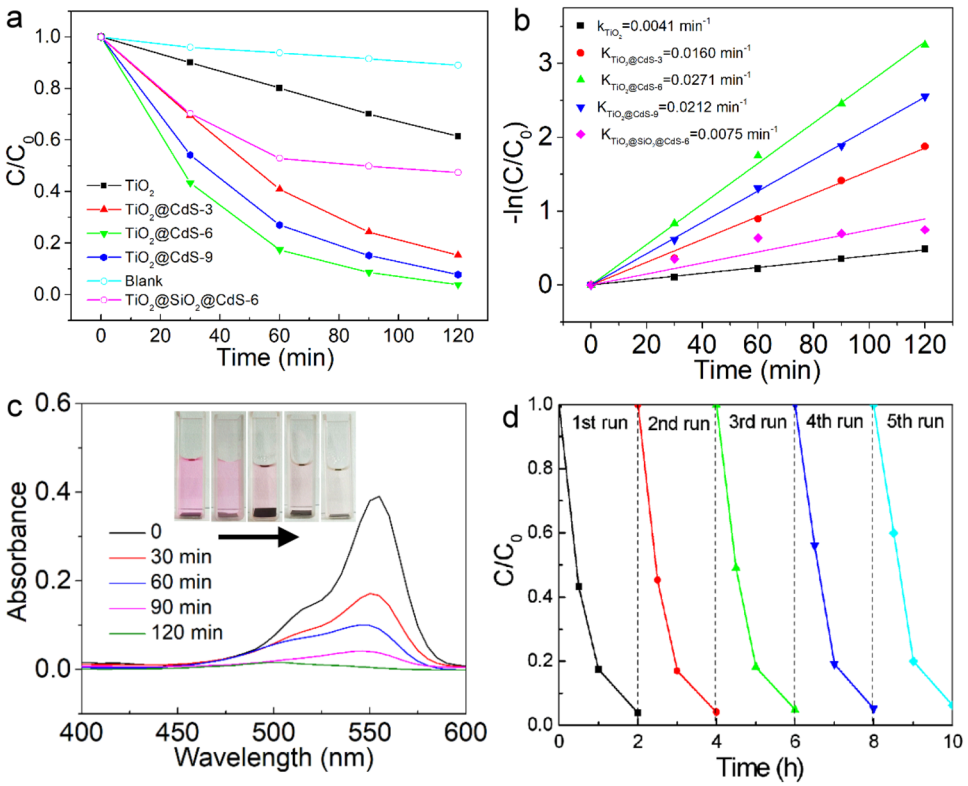

Fig. 8 **a** Photodegradation of RhB water solution and **b** $-\ln(C_0/C)$ versus irradiation time for different photocatalysts, **c** TiO_2@CdS-6 degradation curve and color change, **d** repeated photocatalytic experiments of TiO_2@CdS-6 NRAs

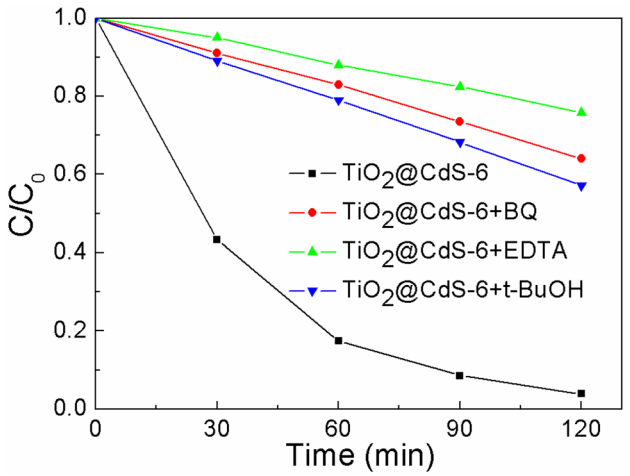

Fig. 9 Trapping experiment of active species using TiO_2@CdS-6 as photocatalyst

edge structure in TiO_2@CdS heterostructure, as shown the mechanism a in Fig. 11. However, the photoinduced electrons of TiO_2 cannot reduce O_2 to form $\cdot O_2^-$ because the conduction band (CB) of TiO_2 is lower than the standard redox potential of $O_2/\cdot O_2^-$. Similarly, photoinduced holes on CdS surface cannot oxidize H_2O to produce $\cdot OH$ radicals because the valence band (VB) of CdS is higher than the standard potential of $OH^-/\cdot OH$ and $H_2O/\cdot OH$ [63]. According to the trapping experiments of reactive species, h^+, $\cdot OH$ and $\cdot O^{2-}$ are involved during the photocatalytic reaction. So, the photocatalytic reaction obeys the mechanism b rather than mechanism a in Fig. 11. This is to say, the photoinduced electrons in CdS tend to keep in the CB of CdS, and the photoinduced holes in TiO_2 remain in the VB of TiO_2. Meanwhile, the photoinduced electrons in the CB of TiO_2 combine with the photoinduced holes in VB of CdS. This is the typical Z-scheme mechanism [32, 64]. In this case, the recombination of photoinduced electron–hole pairs are impeded efficiently and the lifetime of charge carrier in TiO_2@CdS core–shell heterostructure is prolonged. Consequently, the photocatalytic activity of TiO_2@CdS heterostructure NRAs is higher than that of pure TiO_2 NRAs. In addition, TiO_2@CdS-6 NRAs exhibits the best photocatalytic activity among all TiO_2@CdS NRAs. Namely, the optimal thickness of CdS shell is 11 nm. TiO_2@CdS-3 NRAs shows the worse photocatalytic activity than TiO_2@CdS-6 NRAs because the thickness of CdS shell layer in TiO_2@CdS-3 NRAs is relatively thin. For TiO_2@CdS-9 NRAs, the excessively thick CdS shell not only hinders the TiO_2 absorption of sunlight but also restrains the migration of charge carriers between CdS and TiO_2 in TiO_2@CdS NRAs heterostructure.

4 Conclusions

Core–shell structure TiO_2@CdS nanorod arrays with different CdS shell thicknesses were fabricated via solvothermal way and subsequent successive ionic layer adsorption

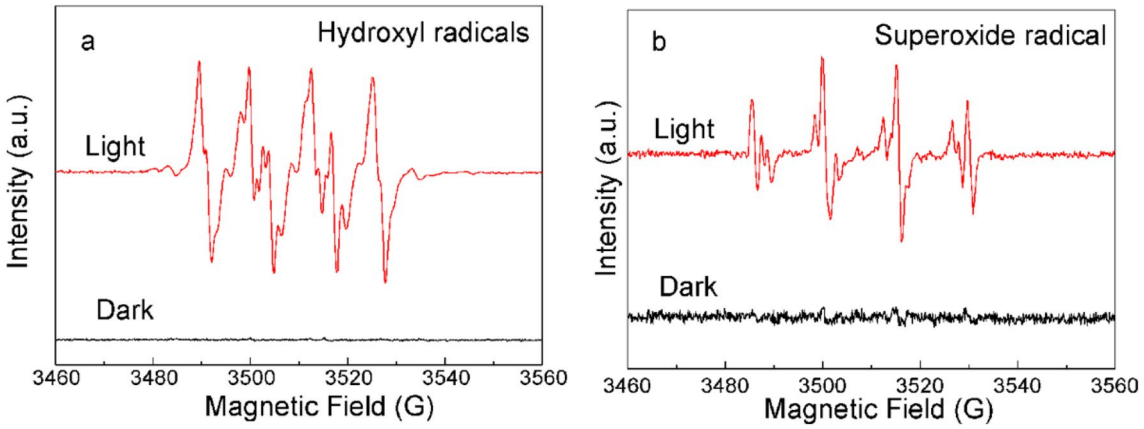

Fig. 10 ESR spectra of radicals trapped by DMPO in the presence of TiO_2@CdS-6 in the dark and under simulated solar irradiation: DMPO–$\cdot O^{2-}$ (**a**), DMPO–$\cdot OH$ (**b**)

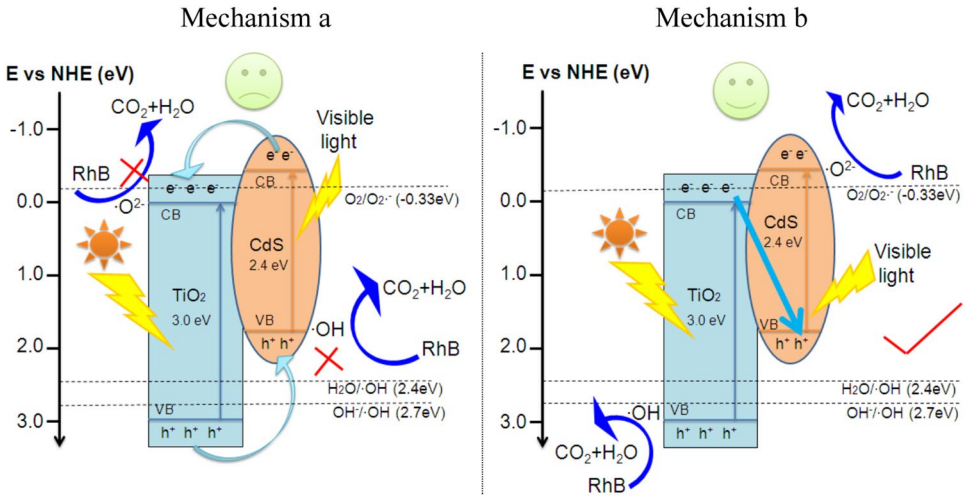

Fig. 11 Photodegradation of RhB and schematic diagram of the energy band structure of TiO_2@CdS heterostructure

and reaction (SILAR) method. The photocatalytic result showed that the photocatalytic activities of all TiO_2@CdS NRAs were drastically enhanced compared to that of pure TiO_2 NRAs under simulated sunlight irradiation. The Z-scheme heterostructure formed by TiO_2@CdS promotes the transport and separation of photogenerated carriers between the interfaces of the two materials, greatly improving the photocatalytic efficiency. Among all TiO_2@CdS NRAs, the thickness CdS shell of 11 nm exhibited the highest photocatalytic activity and good reusability, and their degradation rate constant were about 6.6 times than that of pure TiO_2.

Acknowledgements This work is supported by the National Natural Science Foundation of China (Grant No. 61378085) and the Thirteenth Five-Year Program for Science and Technology of Education Department of Jilin Province (Item No. JJKH20191017KJ).

References

1. Z. Zhu, Z.Y. Lu, D.D. Wang, X. Tang, Y.S. Yan, Construction of high-dispersed Ag/Fe_3O_4/g-C_3N_4 photocatalyst by selective photo-deposition and improved photocatalytic activity. Appl. Catal. B **182**, 115–122 (2016)
2. D.J. Martin, K. Qiu, S.A. Shevlin, A.D. Handoko, X. Handoko, Highly efficient photocatalytic h_2 evolution from water using visible light and structure-controlled graphitic carbon nitride. Angew. Chem. Int. Ed. **53**, 9240–9245 (2014)
3. M. Rafatullah, O. Sulaiman, R. Hashim, A. Ahmad, Adsorption of methylene blue on lowcost adsorbents: a review. J. Hazard. Mater. **177**, 70–80 (2010)
4. C. Namasivayam, D. Kavitha, Removal of Congo Red from water by adsorption onto activated carbon prepared from coir pith, an agricultural solid waste. Dyes Pigm. **54**, 47–58 (2002)
5. J. Zhang, L. Huang, H. Jin, Y. Sun, X. Ma, Constructing two-dimension MoS_2/Bi_2WO_6 core-shell heterostructure as carriers

transfer channel for enhancing photocatalytic activity. Mater. Res. Bull. **85**, 140–146 (2017)
6. Z.F. Jiang, D.L. Jiang, Z.X. Yan, D. Liu, A new visible light active multifunctional ternary composite based on TiO_2-In_2O_3 nanocrystals heterojunction decorated porous graphitic carbon nitride for photocatalytic treatment of hazardous pollutant and H_2 evolution. Appl. Catal. B **170**, 195–205 (2015)
7. X. Li, T. Xia, C.H. Xu, J. Murowchick, X.B. Chen, Synthesis and photoactivity of nanostructured CdS-TiO_2 composite catalysts. Catal. Today **225**, 64–73 (2014)
8. X. Chen, S.S. Mao, Titanium dioxide nanomaterials: synthesis, properties, modifications, and applications. Chem. Rev. **107**, 2891–2959 (2007)
9. C. Zhao, H. Luo, F. Chen, P. Zhang, L. Yi, K. You, A novel composite of TiO_2 nanotubes with remarkably high efficiency for hydrogen production in solardriven water splitting. Energ. Environ. Sci. **7**, 1700–1707 (2014)
10. C.B.D. Marien, T. Cottineau, D. Roberta, P. Drogui, TiO_2 nanotube arrays: influence of tube length on the photocatalytic degradation of Paraquat. Appl. Catal. B **194**, 1–6 (2016)
11. D. Reyes-Coronado, G. Rodr´ıguez-Gattorno, M.E. Espinosa-Pesqueira, C. Cab, R. Coss, G. Oskam, Phase-pure TiO_2 nanoparticles: anatase, brookite and rutile. Nanotechnology **19**, 145605 (2008)
12. M. Dawson, C. Ribeiro, M.R. Morelli, Rutile supported anatase nanostructured films as photocatalysts for the degradation of water contaminants. Ceram. Int. **42**, 808–819 (2016)
13. K. Ozawa, S. Yamamoto, R. Yukawa, R.Y. Liu, N. Terashima, Y. Natsui, H. Kato, K. Mase, I. Matsuda, Correlation between photocatalytic activity and carrier lifetime: acetic acid on single-crystal surfaces of anatase and rutile TiO_2. J. Phys. Chem. C **122**, 9562–9569 (2018)
14. X. Yang, L. Wu, L. Ma, X. Li, T. Wang, S. Liao, Pd nano-particles (NPs) confined in titanate nanotubes (TNTs) for hydrogenation of cinnamaldehyde. Catal. Commun. **59**, 184–188 (2015)
15. R. Daghrir, P. Drogui, D. Robert, Modified TiO_2 for environmental photocatalytic applications: a review. Ind. Eng. Chem. Res. **52**, 3581–3599 (2013)
16. P. Kar, S. Zheng, Y. Zhang, E. Vahidzadeh, A. Manuel, R. Kisslinger, K. Alam, U. Thakur, N. Mahdi, P. Kumar, K. Shankar, High rate CO_2 photoreduction using flame annealed TiO_2 nanotubes. Appl. Catal. B **243**, 522–536 (2019)
17. M. Kobielusz, K. Pilarczyk, E. Swietek, K. Szaciłowski, W. Macyk, Spectroelectrochemical analysis of TiO_2 electronic states-implications on the photocatalytic activity of anatase and rutile. Catal. Today **309**, 35–42 (2018)
18. U. Nwankwo, R. Bucher, A.B.C. Ekwealor, M. Maaza, F.I. Ezema, Synthesis and characterizations of rutile-TiO_2 nanoparticles derived from chitin for potential photocatalytic applications. Vacuum **161**, 49–54 (2019)
19. A. Mohammadpour, B.D. Wiltshire, Y. Zhang, S. Farsinezhad, A.M. Askar, R. Kisslinger, Y. Ren, P. Kar, K. Shankar, 100-fold improvement in carrier drift mobilities in alkanephosphonate-passivated monocrystalline TiO_2 nanowire arrays. Nanotechnology **28**, 144001 (2017)
20. U.K. Thakur, A.M. Askar, R. Kisslinger, B.D. Wiltshire, P. Kar, K. Shankar, Halide perovskite solar cells using monocrystalline TiO_2 nanorod arrays as electron transport layers: impact of nanorod morphology. Nanotechnology **28**, 274001 (2017)
21. D. Sarkar, C.K. Ghosh, S. Mukherjee, Three dimensional Ag_2O/TiO_2 type-II (p-n) nanoheterojunctions for superior photocatalytic activity. ACS Appl. Mater. Interfaces. **5**, 331–337 (2013)
22. Y.S. Chang, M. Choi, M. Baek, P.Y. Hsieh, K.J. Yong, Y.J. Hsu, CdS/CdSe co-sensitized brookite H: TiO_2 nanostructures: charge carrier dynamics and photoelectrochemical hydrogen generation. Appl. Catal. B **225**, 379–385 (2018)
23. T. Lv, L.K. Pan, X.J. Liu, Z. Sun, Visible-light photocatalytic degradation of methyl orange by CdS-TiO_2-Au composites synthesized via microwave-assisted reaction. Electrochim. Acta **83**, 216–220 (2012)
24. N. Mohaghegh, B. Eshaghi, E. Rahimi, M.R. Gholami, Ag_2CO_3 sensitized TiO_2 nanoparticles prepared in ionic liquid medium: a new Ag_2CO_3/TiO_2/RTIL heterostructure with highly efficient photocatalytic activity. J. Mol. Catal. A **406**, 152–158 (2015)
25. J. Zhang, X.M. Ma, L.L. Zhang, Z.D. Lu, Constructing a novel n-p-n dual heterojunction between anatase TiO_2 nanosheets with coexposed 101}, {001 facets and porous ZnS for enhancing photocatalytic activity. J. Phys. Chem. C **121**, 6133–6140 (2017)
26. Y.B. Liu, H.B. Zhou, B.X. Zhou, J.H. Li, H.C. Chen, J.J. Wang, J. Bai, Highly stable CdS-modified short TiO_2 nanotube array electrode for efficient visible-light hydrogen generation. Int. J. Hydrog. Energy **36**, 167–174 (2011)
27. Y. Lin, J. Song, Y. Ding, S. Lu, Z.L. Wang, Alternating the output of a CdS nanowire nanogenerator by a white-light-stimulated optoelectronic effect. Adv. Mater. **20**, 3127–3130 (2008)
28. Y. Liu, P. Zhang, B.Z. Tian, J.L. Zhang, Enhancing the photocatalytic activity of CdS nanorods for selective oxidation of benzyl alcohol by coating amorphous TiO_2 shell layer. Catal. Commun. **70**, 30–33 (2015)
29. W.H. Dong, F. Pan, L.L. Xu, M.R. Zheng, C.H. Sow, K. Wu, G.Q. Xu, W. Chen, Facile synthesis of CdS@TiO_2 core-shell nanorods with controllable shell thickness and enhanced photocatalytic activity under visible light irradiation. Appl. Surf. Sci. **349**, 279–286 (2015)
30. C. Su, C. Shao, Y. Liu, Electrospun nanofibers of TiO_2/CdS heteroarchitectures with enhanced photocatalytic activity by visible light. J. Colloids Interface Sci. **359**, 220–227 (2011)
31. X.Y. Guo, C.F. Chen, W.Y. Song, X. Wang, W.H. Di, W.P. Qin, CdS embedded TiO_2 hybrid nanospheres for visible light photocatalysis. J. Mol. Catal. A **387**, 1–6 (2014)
32. P. Gao, J. Liu, T. Zhang, D.D. Sun, W. Ng, Hierarchical TiO_2/CdS "spindle-like" composite with high photodegradation and antibacterial capability under visible light irradiation. J. Hazard. Mater. **229–230**, 209–216 (2012)
33. Y. Zhang, Y. Gao, X.H. Xia, Q.R. Deng, M.L. Guo, Structural engineering of thin films of vertically aligned TiO_2 nanorods. Mater. Lett. **64**, 1614–1617 (2010)
34. H. Pan, J.S. Qian, A. Yu, M.G. Xu, TiO_2 wedgy nanotubes array flims for photovoltaic enhancement. Appl. Surf. Sci. **257**, 5059–5063 (2011)
35. Y.T. Xue, Z.S. Wu, X.F. He, X. Yang, X.Q. Chen, Z.Z. Gao, Constructing a Z-scheme heterojunction of egg-like core@shell CdS@TiO_2 photocatalyst via a facile reflux method for enhanced photocatalytic performance. Nanomaterials **9**, 222 (2019)
36. C.J. Liu, Y.H. Yang, J. Li, S. Chen, Phase transformation synthesis of TiO_2/CdS heterojunction film with high visible-light photoelectrochemical activity. Nanotechnology **29**, 265401 (2018)
37. E. Uzer, P. Kumar, R. Kisslinger, P. Kar, U.K. Thakur, S. Zeng, K. Shankar, T. Nilges, Vapor deposition of semiconducting phosphorus allotropes into TiO_2 nanotube arrays for photoelectrocatalytic water splitting. ACS Appl Nano Mater **26**, 3358–3367 (2019)
38. M. Xi, Y.L. Zhang, L.Z. Long, X.J. Li, Controllable hydrothermal synthesis of rutile TiO_2 hollow nanorod arrays on $TiCl_4$ pretreated Ti foil for DSSC application. J. Solid State Chem. **219**, 118–126 (2014)
39. P. Kumar, U.K. Thakur, K. Alam, P. Kar, R. Kisslinger, S. Zeng, S. Patel, K. Shankar, Arrays of TiO_2 nanorods embedded with fluorine doped carbon nitride quantum dots (CNFQDs) for visible light driven water splitting. Carbon **137**, 174–187 (2018)
40. P. Kar, Y. Zhang, S. Farsinezhad, A. Mohammadpour, B.D. Wiltshire, H. Sharma, K. Shankar, Rutile phase n-and p-type anodic

titania nanotube arrays with square-shaped pore morphologies. Chem. Commun. **51**, 7816–7819 (2015)
41. S.S. Mali, S.K. Desai, D.S. Dalavi, C.A. Betty, P.N. Bhosalea, P.S. Patil, CdS sensitized TiO_2 nanocorals: hydrothermal synthesis, characterization, application. Photochem. Photobiol. Sci. **10**, 1652–1658 (2011)
42. P.P. Zhou, Y. Xie, J. Fang, Y. Ling, C.L. Yu, X.M. Liu, Y.H. Dai, Y.C. Qin, D. Zhou, CdS quantum dots confined in mesoporous TiO_2 with exceptional photocatalytic performance for degradation of organic pollutants. Chemosphere **178**, 1–10 (2017)
43. N. Qin, J.H. Xiong, R.W. Liang, Y.H. Liu, S.Y. Zhang, Y.H. Li, Z.H. Li, L. Wu, Highly efficient photocatalytic H_2 evolution over MoS_2/CdS-TiO_2 nanofibers prepared by an electrospinning mediated photodeposition method. Appl. Catal. B **202**, 374–380 (2017)
44. S. David, M.A. Mahadik, H.S. Chung, J. Ryu, J.S. Jang, Facile hydrothermally synthesized a novel CdS nanoflower/rutile-TiO_2 nanorod heterojunction photoanode used for photoelectrocatalytic hydrogen generation. ACS Sustain. Chem. Eng. **5**, 7537–7548 (2017)
45. S.Y. Li, Z.L. Liu, G.X. Xiang, B.H. Ma, X.D. Meng, Y.L. He, Influence of calcination temperature on the photocatalytic performance of the hierarchical TiO_2 pinecone-like structure decorated with CdS nanoparticles. Ceram. Int. **45**, 767–776 (2019)
46. Y.F. Li, L.L. Wang, Z.L. Li, Y.L. Liu, Z.Y. Peng, Synthesis and photocatalytic property of V_2O_5@TiO_2 core-shell microspheres towards gaseous benzene. Catal. Today **321–322**, 164–171 (2019)
47. H.Y. Yang, Z.L. Liu, K. Wang, S.T. Pu, S.N. Yang, L. Yang, A facile synthesis of TiO_2-CdS heterostructures with enhanced photocatalytic activity. Catal. Lett. **147**, 2581–2591 (2017)
48. P.S. Shinde, J.W. Park, M.A. Mahadik, J. Ryu, J.H. Park, Y.J. Yi, J.S. Jang, Fabrication of efficient CdS nanoflowers-decorated TiO_2 nanotubes array heterojunction photoanode by a novel synthetic approach for solar hydrogen production. Int. J. Hydrog. Energy **46**, 21078–21087 (2016)
49. G.D. Yang, B.L. Yang, T.C. Xiao, Z.F. Yan, One-step solvothermal synthesis of hierarchically porous nanostructured CdS/TiO_2 heterojunction with higher visible light photocatalytic activity. Appl. Surf. Sci. **283**, 402–410 (2013)
50. M. Fujishima, Y. Nakabayashi, K. Takayama, H. Kobayashi, H. Tada, High coverage formation of CdS quantum dots on TiO_2 by the photocatalytic growth of preformed seeds. J. Phys. Chem. C **120**, 17365–17371 (2016)
51. X.Y. Li, D.X. Liu, Z. Shi, J.H. Yang, Effect of Ag_2S shell thickness on the photocatalytic properties of ZnO/Ag_2S core-shell nanorod arrays. J. Mater. Sci. **54**, 1226–1235 (2019)
52. X.Y. Li, X. Li, B.Y. Zhu, J.S. Wang, H.X. Lan, X.B. Chen, Synthesis of porous ZnS ZnO and ZnS/ZnO nanosheets and their photocatalytic properties. RSC Adv. **7**, 30956–30962 (2017)
53. Y.H. Zhang, N. Zhang, Z.R. Tang, Y.J. Xu, Identification of Bi2WO6 as a highly selective visible-light photocatalyst toward oxidation of glyceroltodihy-droxyacetone in water. Chem. Sci. **4**, 1820–1824 (2013)
54. C.L. Cao, C.G. Hu, W.D. Shen, S.X. Wang, Y.S. Tian, X. Wang, Synthesis and characterization of TiO_2/CdS core–shell nanorod arrays and their photoelectrochemical property. J. Alloys Compd. **523**, 139–145 (2012)
55. X. Li, C.Y. Liu, D.Y. Wu, J.Z. Li, P.W. Huo, H.Q. Wang, Improved charge transfer by size-dependent plasmonic Au on C_3N_4 for efficient photocatalytic oxidation of RhB and CO_2 reduction. Chin. J. Catal. **40**, 928–939 (2019)
56. D. Li, C. Shen, J.Z. Liu, Y.J. Li, X.H. Zhou, P.W. Song, H.Q. Huo, Y.S. Wang, Yan, Fabricated rGO-modified Ag_2S nanoparticles/g-C_3N_4 nanosheets photocatalyst for enhancing photocatalytic activity. J. Colloids Interface Sci. **554**, 468–478 (2019)
57. Y.Y. Lu, Y.Y. Zhang, J. Zhang, Y. Shi, Z. Li, Z.C. Feng, C. Li, In situ loading of CuS nanoflowers on rutile TiO_2 surface and their improved photocatalytic performance. Appl. Surf. Sci. **370**, 312–319 (2016)
58. X.Y. Li, D.X. Liu, B.Y. Zhu, J. Wang, J.H. Lang, Facile preparation of ZnO/Ag_2CO_3 heterostructured nanorod arrays with improved photocatalytic activity. J. Phys. Chem. Solids **125**, 96–102 (2019)
59. D.D. Wang, D.L. Han, Z. Shi, J. Wang, J.H. Yang, X.Y. Li, H. Song, Optimized design of three-dimensional multi-shell Fe_3O_4/SiO_2/ZnO/ZnSe microspheres with type II heterostructure for photocatalytic applications. Appl. Catal. B **227**, 61–69 (2018)
60. H.R. Liu, H.F. Zhai, C.J. Hu, J.E. Yang, Z.Y. Liu, Hydrothermal synthesis of In_2O_3 nanoparticles hybrid twins hexagonal disk ZnO heterostructures for enhanced photocatalytic activities and stability. Nanoscale Res. Lett. **12**, 466–476 (2017)
61. H.R. Liu, Y.C. Hu, Z.X. Zhang, X.G. Liu, H.S. Jia, B.S. Xu, Synthesis of spherical Ag/ZnO heterostructural composites with excellent photocatalytic activity under visible light and UV irradiation. Appl. Surf. Sci. **355**, 644–652 (2015)
62. H.X. Zhao, S. Cui, L. Yang, G.D. Li, N. Li, X.T. Li, Synthesis of hierarchically meso-macroporous TiO_2/CdS heterojunction photocatalysts with excellent visible-light photocatalytic activity. J. Colloids Interface Sci. **23**, 4246–4254 (2013)
63. W. Wu, C.Z. Jiang, V.A.L. Roy, Recent progress in magnetic iron oxide-semiconductor composite nanomaterials as promising photocatalysts. Nanoscale **7**, 38–58 (2015)
64. Y.X. Zhu, Y.F. Wang, Z. Chen, L.S. Qin, L.B. Yang, L. Zhu, Visible light induced photocatalysis on CdS quantum dots decorated TiO_2 nanotube arrays. Appl. Catal. A **498**, 164–171 (2015)